Canadian Geotechnical Journal

OPEN ACCESS | Research Article

An evaluation of *p–y* curves for fatigue analysis of offshore piles and conductors

M. Guevara[a], **J.P. Doherty**[b], **P.G. Watson**[a], **and D.J. White**[c]

[a]Oceans Graduate School, The University of Western Australia, 35 Stirling Highway, 6009 Perth, Australia; [b]School of Civil, Environmental and Mining Engineering, The University of Western Australia, 35 Stirling Highway, 6009 Perth, Australia; [c]School of Engineering, University of Southampton, Burgess Road, Southampton SO16 7QF, UK

Corresponding author: **M. Guevara** (email: mariajoseguevarac@gmail.com)

Abstract

The paper evaluates methods for deriving *p–y* curves for fatigue analysis of slender piles and conductors. Updated ISO standard guidance is compared to a new approach, which is validated by centrifuge tests and based on laboratory measurements of stiffness. This new approach provides a more accurate match to previously-published data on which the ISO guidelines are based. Additionally, a third method is examined—the parallel-Iwan critical state inspired (PICSI) framework—which captures changes in *p–y* response through cyclic loading and consolidation. Bending moments from a pile–soil Finite Element (FE) analysis using the three methods are compared to data from flexible piles centrifuge testing. Load history effects are evident, with the bending moment profile for a given cyclic amplitude being altered by prior larger cycles, through a changing *p–y* response. The resulting evolution of the bending moment profile showed migration of the fatigue hotspot along the pile, which improves fatigue life. Whereas the ISO fatigue *p–y* curves over-predicted the observed stiffness, the alternative simplified *p–y* method matched the bending moments to ±25% accuracy, and the PICSI framework gave the most accurate bending moment predictions across the full test sequence. These latter two methods are recommended for design use in preference to the ISO approach.

Key words: fatigue, soil/structure interaction, cyclic loading, laterally loaded piles, *p–y* curves

Résumé

L'article évalue les méthodes de dérivation des courbes p-y pour l'analyse de la fatigue des pieux élancés et des colonnes montantes. La directive mise à jour de la norme ISO est comparée à une nouvelle approche, validée par des essais en centrifugeuse et fondée sur des mesures de rigidité en laboratoire. Cette nouvelle approche offre une correspondance plus précise avec les données publiées antérieurement sur lesquelles reposent les lignes directrices de la norme ISO. De plus, une troisième méthode est examinée – le cadre PICSI – qui permet de saisir les variations de la réponse p-y sous l'effet du chargement cyclique et de la consolidation. Les moments de flexion issus d'une analyse éléments finis pieu-sol utilisant les trois méthodes sont comparés aux données provenant d'essais en centrifugeuse sur des pieux flexibles. Les effets de l'historique de chargement sont évidents : le profil du moment de flexion pour une amplitude cyclique donnée est modifié par des cycles antérieurs de plus grande amplitude, en raison de l'évolution de la réponse p-y. L'évolution du profil du moment de flexion observée a révélé une migration du point critique de fatigue le long du pieu, ce qui améliore la durée de vie en fatigue. Alors que les courbes p–y de fatigue selon la norme ISO surestimaient la rigidité observée, la méthode p–y simplifiée alternative a permis de reproduire les moments de flexion avec une précision de ±25 %, et le cadre PICSI a fourni les prévisions les plus précises des moments de flexion pour l'ensemble de la séquence d'essais. Ces deux dernières méthodes sont recommandées pour une utilisation en conception de préférence à l'approche ISO.

Mots-clés : fatigue, interaction sol-structure, chargement cyclique, pieux chargés latéralement, courbes p–y

Introduction

Estimating the fatigue life of a slender member such as a pile or a drilling conductor is a critical design consideration among the various checks that must be performed to ensure safe operations. In a drilling system, in addition to providing axial support to the system and preventing the walls of the hole from collapsing, conductors transfer the lateral displacements from the upper parts of the system to the soil. Due to the system being interconnected through the riser and tensioned from the vessel (Fig. 1), the environmental displacements experienced by the vessel on top of the system are transferred down to the conductor as cyclic displacements.

Fig. 1. Modelling lateral soil–pile/conductor interaction with *p*–*y* curves.

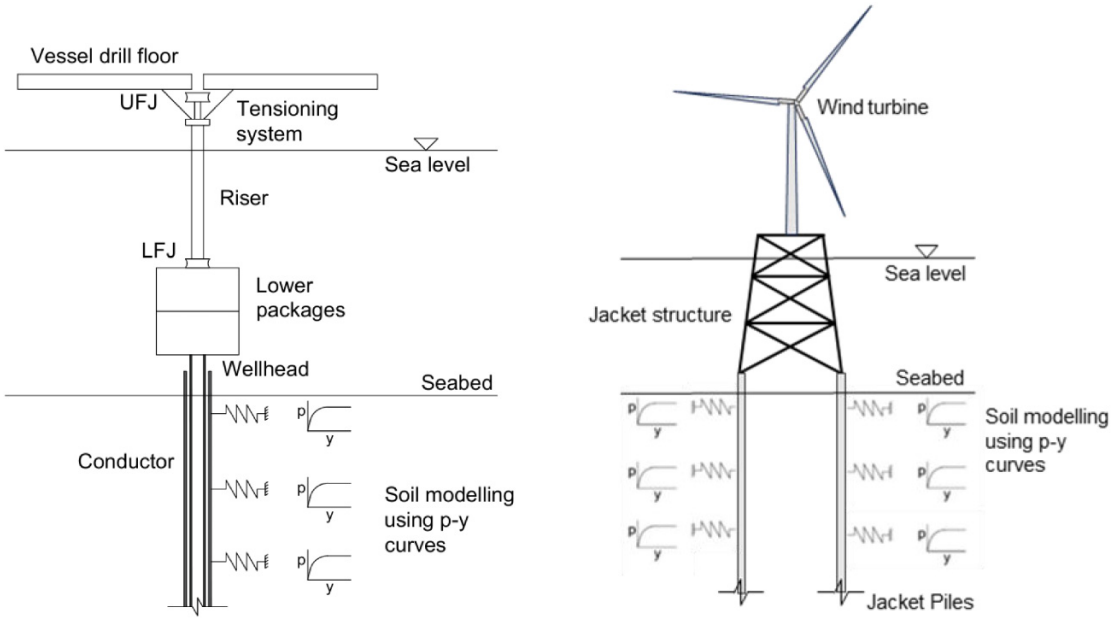

Similarly, piles or pile groups supporting offshore structures suffer continuous lateral loading from waves and wind loading, leading to a requirement to assess fatigue—while this paper focused on the case of a drilling conductor, findings are equally valid to the pile jacket scenario.

In design, stresses are tracked at the locations considered most at risk of fatigue failure. These are called hotspots and include locations where there are changes in geometry, discontinuities, connectors, or welds.

Conductors are typically pipe piles with diameters (d) between 30″ and 36″, wall thickness around 1″, and length (L) to diameter (d) ratios > 20. Due to the large L/d ratios, conductors can be accurately represented as Euler–Bernoulli beams, and the soil–conductor lateral load–displacement relationship modelled as Winkler springs. The most widely used type of Winkler spring for lateral behaviour of conductors is the *p*–*y* curve, which is a nonlinear relationship between soil resistance per unit length of pile ($P = pd$) and lateral displacement (y), where p is the nominal lateral pressure on the pile. The secant stiffness k of a *p*–*y* curve at any given point is defined as

$$(1) \qquad k = \frac{P}{y} = \frac{p}{y/d}$$

Current ISO 19901-4 guidelines (ISO 2016) recommend *p*–*y* curves based on monotonic loading that are known to underestimate stiffness (Jeanjean 2009), particularly at small displacements. For drilling operations, displacements at the conductor head are typically <10% of the diameter (Jeanjean 2009; Zakeri et al. 2016; Komolafe and Aubeny 2020); therefore, accurate determination of stiffness at displacements less than 0.10 d is important for reliable fatigue life estimation.

The forthcoming edition of ISO 19901-4 (ISO/DIS 2022) has been through public review, and proposes new *p*–*y* models to overcome previous limitations, with different *p*–*y* curves for different design conditions—monotonic, cyclic, and fatigue:

- The recommended *p*–*y* curves for monotonic loading in clay (originally from Jeanjean et al. 2017) can be derived by either scaling from simple shear laboratory tests or by using default normalised curves.
- The *p*–*y* curves for fatigue analysis of conductors are intended to represent "steady state" conditions, which assume that there is a unique unload–reload stiffness for a given displacement, reached after a few hundred cycles, and for which the stiffness and damping are constant. The method disregards the transient phase before reaching this state, as well as the impact of any load history previously experienced, and any potential regain in stiffness due to pore pressure dissipation (consolidation). The method is based on Zakeri et al. (2019), which relies on centrifuge tests performed in Gulf of Mexico and kaolin clay (Zakeri et al. 2016), as well as *p*–*y* apparatus tests (Zakeri et al. 2017) on a range of marine clays.

The methods to derive *p*–*y* curves in the ISO/DIS (2022) will be referred to as the "ISO" methods from this point onward, and distinction will be made whether the reference is to the monotonic or the fatigue method. The cyclic method proposed in the ISO/DIS (2022) is intended to be used to predict pile behaviour under extreme (design) storm loads. This is different to the operational loads that are experienced during drilling, and hence the cyclic method is not relevant and not considered further.

Recent studies (Doherty et al. 2019; Guevara et al. 2020, 2021; Zhang et al. 2011) have demonstrated the impact of episodic cyclic loading and pore pressure dissipation on the soil–pile stiffness around short rigid piles in reconstituted carbonate silt and kaolin clay. Such changes in stiffness af-

fect the stresses in a pile or conductor by progressively shifting the location of peak bending moments (BMs) as the soil stiffness changes.

White et al. (2022) proposed a framework to model the effect of load history on *p*–*y* curves, by simultaneously accounting for softening due to cyclic remoulding and recovery due to dissipation of pore pressures. The framework is inspired by critical state soil mechanics (Wood 1990), and incorporates additional features observed in experiments. It was developed for soils that tend to densify with shearing, such as clays or silts with an initial state on the "wet" side of the critical state line.

For fatigue analysis the BM at hot-spots is critical in design, so this paper aims to assess the performance of the ISO fatigue method when used to compute the BMs from centrifuge tests on a flexible pile. In addition, two other methods are also used to compute the BMs. In summary, three approaches for defining *p*–*y* curves for fatigue analysis in soft soils are examined:

- the ISO (ISO/DIS 2022) method for fatigue *p*–*y* curves;
- a new simplified fully remoulded "steady-state" method proposed in this paper, based on centrifuge data and laboratory element tests; and
- the parallel-Iwan critical state inspired (PICSI) method (White et al. 2022).

The impact of the choice of *p*–*y* curve on the BM profile is discussed and recommendations for fatigue design of conductors in soft soils provided.

p–*y* curves: ISO guidelines

Lateral ultimate soil resistance

The overall approach for pile monotonic *p*–*y* modelling in the ISO method harmonises various design procedures (Randolph and Houlsby 1984; Murff and Hamilton 1993; Yu et al. 2015; Zhang et al. 2016) and accounts for pile roughness, gap formation behind the pile, and the combination of deep flow-around and shallow wedge failure mechanisms. The ultimate lateral soil reaction pressure ($p_u = N_p.s_u$) is an input for developing the monotonic, fatigue, and cyclic *p*–*y* curves. The method was calibrated using stress–strain behaviour measured in direct simple shear tests at a strain rate of 5%/h, so the guidelines recommend that s_u determined from Simple Shear testing (DSS) is used.

Monotonic *p*–*y* curves

Two approaches are proposed for the shape of the *p*–*y* curves: (1) default normalised p/p_u versus y/d curves that depend on plasticity index and OCR, and (2) a scaling procedure from simple shear tests. The scaling procedure is based on Zhang and Andersen (2017), recognising similarities between the soil stress–strain response and the *p*–*y* curves as demonstrated by Bransby (1999). While these *p*–*y* curves are proposed for monotonic conditions where the large displacements are expected, their suitability for conductor fatigue life estimation is discussed in this paper.

Fig. 2. Normalised fatigue *p*–*y* curve.

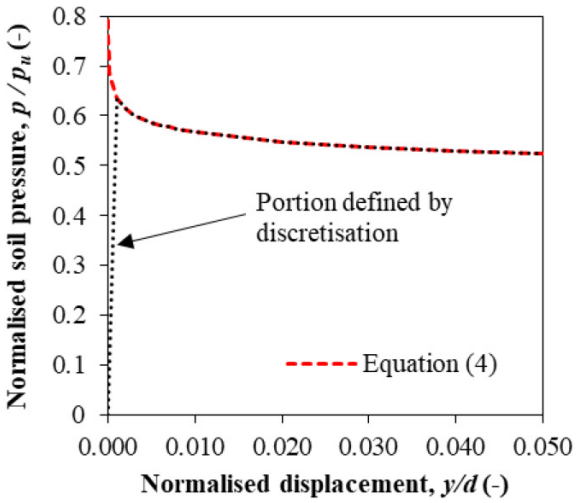

Fatigue *p*–*y* curves

The ISO method for fatigue analysis is based on experiments performed in kaolin clay and Gulf of Mexico clay, and validated with data from *p*–*y* apparatus tests on a range of marine clays (Zakeri et al. 2016, 2019). The test data were used to define a normalised "steady-state" secant stiffness (*K*), which is defined as the peak-to-peak secant stiffness within a loop ($k_{p\text{-}p}$) normalised by p_u:

$$K = \frac{k_{p-p}}{p_u} \quad (2)$$

and where

$$k_{p-p} = \frac{\Delta p}{\Delta y/d} \quad (3)$$

with Δp being the range of lateral soil reaction and Δy being the lateral peak-to-peak movement amplitude.

The guideline provides two options for fatigue *p*–*y* curves: a spring-only method and a spring–dashpot method. In this paper we discuss the spring-only method, which consists of a unique normalised soil response for fatigue actions p_{fa}/p_u represented by

$$p_{fa} = p_u A_s \left(\frac{y}{d}\right)^{-B_s} \quad (4)$$

and where $A_s = 0.45$ if $s_u < 40$ kPa (and $A_s = 0.19$ for other conditions) and $B_s = 0.05$ for all conditions, are the recommended parameters for soft to very hard clay. Equation 4 does not pass through the ($y = 0$, $p = 0$) origin, which is addressed by specifying a point ($\frac{y}{d} = 0.001$) at which the curve given by eq. 4 is joined to the origin (Fig. 2).

When implemented in a numerical soil–pile model, all *p*–*y* springs have to "climb" through this arbitrarily defined portion of the *p*–*y* curve to find convergence for the imposed loads at each timestep. In most fatigue simulations, the mobilised pressure will remain below the peak, so the response is defined largely by the (arbitrary) discretisation of the

Fig. 3. Normalised fully softened secant stiffness from *p*–*y* apparatus and centrifuge tests.

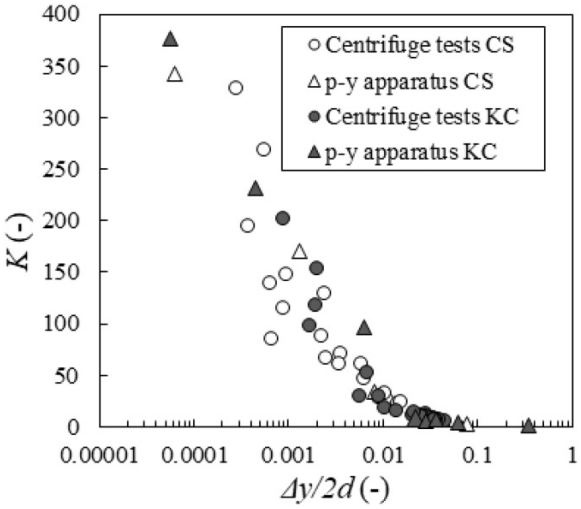

Fig. 4. Measured G_{max} from bender element tests on reconstituted carbonate silt.

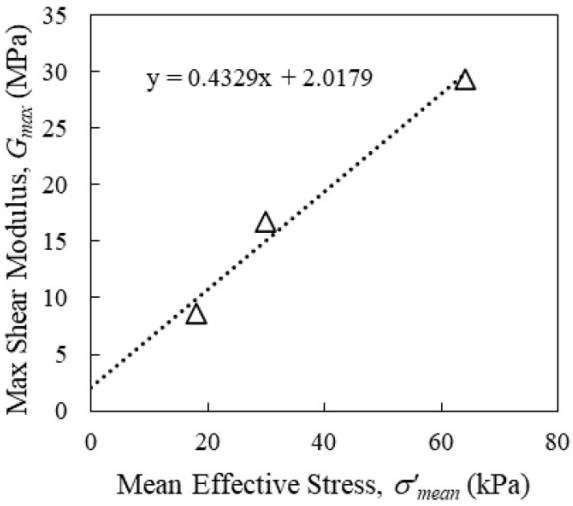

p–*y* curve rather than the data points used to establish the curve. This portion is demonstrably too stiff: the gradient of the initial portion of the curve is $(p/p_u)/(y/d) = 640$. Adopting $p_u \approx 12s_u$ (Jeanjean 2009), the initial portion of the curve can be expressed as

$$(5) \quad p \approx 12s_u 640 \left(\frac{y}{d}\right)$$

Elastic solutions for lateral pile displacement (e.g., Baguelin et al. 1977) suggest that

$$(6) \quad p \approx 4G \left(\frac{y}{d}\right)$$

where G is shear modulus. Substituting eq. 5 into eq. 6 leads to a soil rigidity index of $G/s_u = 1900$, which is much higher than reported values for most normally consolidated soils (Vardanega and Bolton 2013) particularly given that this portion of the curve applies up to 64% of the unsoftened capacity ($p/p_u = 0.64$).

Alternative simplified method

Alternatively, the steady-state *p*–*y* stiffness can be tied to laboratory measurements of small-strain stiffness G_{max}, with the stiffness decaying with amplitude according to a conic form of *p*–*y* curve calibrated to model tests. Recent studies (Guevara et al. 2020, 2022*b*) highlight the similarity between the variation of K with y/d and the variation of G with shear strain, γ, as highlighted in Fig. 3 by data from centrifuge tests and the NGI-operated *p*–*y* apparatus (Zakeri et al. 2017) on reconstituted Carbonate Silt (CS) and Kaolin Clay (KC).

The normalised maximum secant *p*–*y* stiffness at small displacements close to the elastic range, K_{max}, is linked to G_{max} by eqs. 2, 3, and 6:

$$(7) \quad K_{max} = \frac{4G_{max}}{p_u}$$

For the carbonate silt, bender element data provided in Guevara et al. (2022*a*), and supplemented with additional data provided here, show a linear trend for G_{max} with mean effective stress. Note that the data provided here come from testing of specimens prepared with the same stress history as the centrifuge test sample in Guevara et al. (2022*a*). $G_{max} = 4.72$ MPa is indicated for the stress level at 1.8 m depth (Fig. 4), which when combined with $s_u = 2.72$ kPa (measured in simple shear tests at slow rate) and $N_p = 14$ (adjusted for rate effects in the centrifuge pile tests) gives $K_{max} = 495$. This is consistent with the data in Fig. 3, allowing for the minor influence on eq. 6 from other factors including soil–pile relative stiffness, pile length, and head fixity (Baguelin et al. 1977). Values of K_{max} between 370 and 620 are realistic, which is consistent with the data in Fig. 3, showing that soil element test stiffness data from bender elements can be scaled using elastic theory to the limiting *p*–*y* stiffness in model tests.

The test data in Fig. 3 can be fitted using a modification of the four-parameter conic *p*–*y* equation proposed by Burd et al. (2019), which can be differentiated to give the normalised secant stiffness:

$$(8) \quad \frac{p_f}{p_u} = \frac{p_{rem}}{p_u} \frac{2c}{-b + \sqrt{b^2 - 4ac}}; \quad \frac{y}{d} \leq \frac{y_{rem}}{d}$$

where

$$(9) \quad a = 1 - 2n$$

$$(10) \quad b = 2n \frac{y/d}{y_{rem}/d} - (1 - n)\left(1 + \frac{K_{max}\, y/d}{p_{rem}/p_u}\right)$$

$$(11) \quad c = \frac{K_{max}\, y/d}{y_{rem}/d}(1 - n) - n\frac{(y/d)^2}{(y_{rem}/d)^2}$$

and where p_f is the lateral soil pressure for fatigue actions, p_{rem}/p_u is the normalised fully remoulded, i.e., steady state, soil resistance, assumed as equal to $1/S_t$, y_{rem}/d is the normalised displacement at which p_{rem}/p_u is reached, and n is a parameter that determines the shape of the response.

Fig. 5. Normalised fully softened secant stiffness from *p–y* apparatus and centrifuge tests in a range of clays. Data from Guevara et al. (2022*b*) and Zakeri et al. (2019).

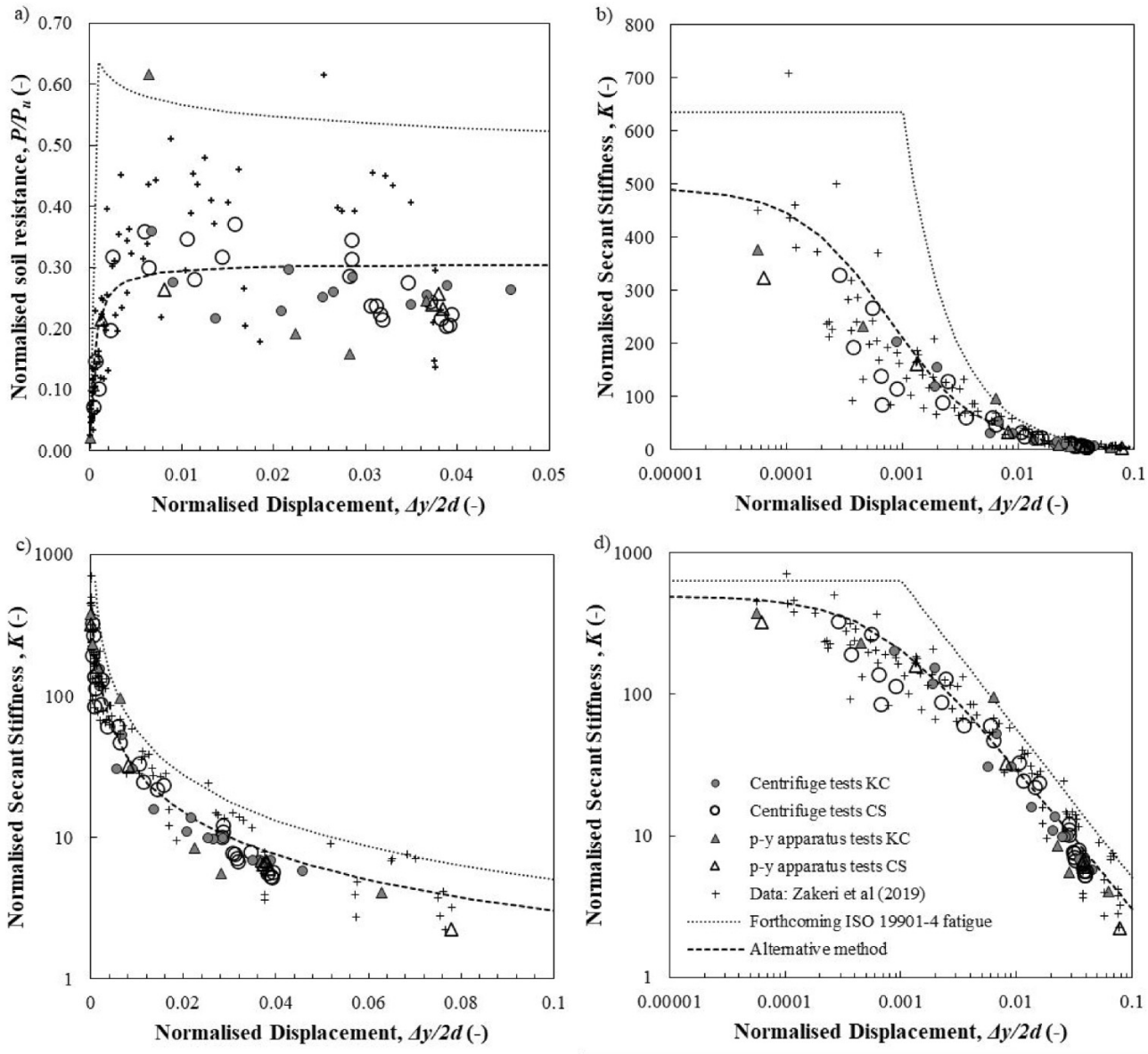

When $y > y_{rem}$ then

(12) $$p_f = p_{rem}$$

Considering the sensitivity $S_t = 3.3$ for the carbonate silt (Guevara et al. 2022*b*) and $K_{max} = 495$ as calculated above, the parameters y_{rem} and n can be adjusted to fit the data in Fig. 3 as shown in Figs. 5*a* and 5*b*, respectively, adopting best fit values of $n = 0.4$ and $y_{rem}/d = 0.05$. The selection of values for these parameters for design should ideally be based on tests results (i.e., resonant columns, cyclic simple shear tests, centrifuge tests, and/or *p–y* apparatus tests). For comparison, the ISO fatigue *p–y* curve is also shown. The displacement axis scale is normalised as $\Delta y/2d$ to be consistent with previous publications, noting that Δy refers to the peak-to-peak movement.

The data from both sources are consistent, even though the data from Zakeri et al. (2019) were normalised assuming $p_u = 12\ s_u$ instead of a test-specific measurement of p_u. Higher values of p_u are possible in *p–y* apparatus testing, which if used would bring the data further into alignment (Guevara et al. 2022*b*).

Figure 5 demonstrates how the perception of data agreement with a fitted curve changes depending on whether a logarithmic axis is applied. At displacements < $0.01d$ the ISO method fatigue *p–y* curve clearly overpredicts the normalised secant stiffness, in some cases by a factor > 2 (Fig. 5*a*). However, this discrepancy is difficult to distinguish when plotting the data on joint logarithmic axes (Fig. 5*d*), and even harder to note when only the secant stiffness axis is logarithmic (Fig. 5*c*).

Fig. 6. (*a*) Illustration of centrifuge setup and (*b*) LAP model.

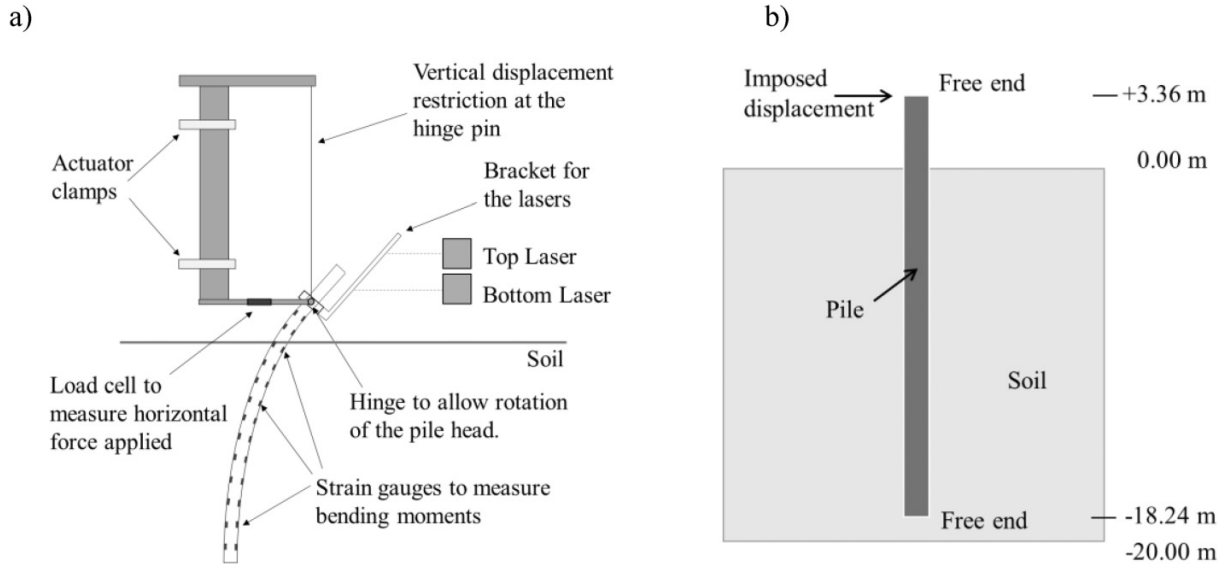

Fig. 7. Applied displacements at pile head in prototype scale.

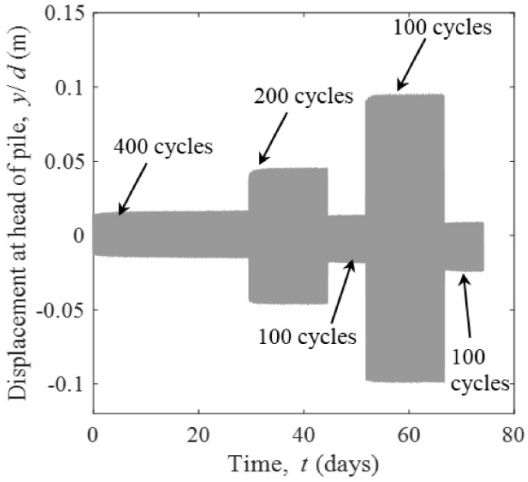

Fig. 8. Bending moment profiles at peak of cycle 1.

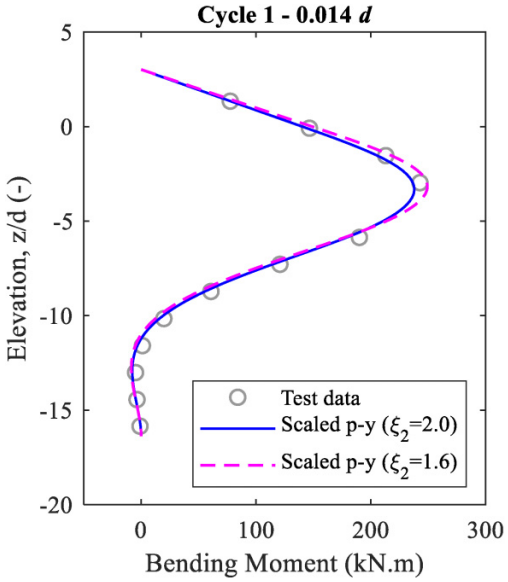

The PICSI method

The PICSI framework described in White et al. (2022) was developed to model changes in a *p*–*y* response due to cyclically-induced remoulding and pore pressure dissipation. The method consists of a parallel-Iwan (PI) system of springs and sliders to model the nonlinear hysteretic behaviour of the *p*–*y* curve, with the strength and stiffness affected by the load history. The approach is applicable for soils that lie on the "wet" side of the critical state line and so densify with shearing and consolidation. Unlike pore pressure accumulation procedures, the system is affected at every timestep by the last increment of displacement and time. This allows the processes of damage, reconsolidation, and densification (or hardening) to occur in parallel.

Using PICSI involves first transforming a *p*–*y* curve into a PI system, applying the first increment of displacement for a given interval of time (δy, δt), and calculating the new strength and stiffness of the PI system based on the soil parameters introduced in the model. This process is repeated for the entire time–displacement history, with the full method described by White et al. (2022) and a calibration procedure set out by Guevara et al. (2023).

Table 1. Parallel-Iwan critical state inspired model parameters for carbonate silt (from Guevara et al. 2023).

Model feature	Description	Parameter	Carbonate silt
Strength limits	Slope of Damage = 0 line	λ^*	8.69
Damage generation	Rate constant	d_r	2.39
	Power constant	d_p	1.68
	Effect of amplitude	d_a	1.00
Pore pressure dissipation	Rate constant	c_r	0.30
	Power constant	c_p	9.65
Hardening	Slope of hardening path	κ^*	0.31
	Variation of hardening slope	h_p	0.002

Table 2. Percentage of pore pressures dissipated by the end of the test.

Packet #	Cyclic amplitude at hinge level (d)	Time from start of test to midpoint of packet (days)	Time from midpoint of packet to end of test (days)	Pore pressure dissipated at the end of test from midpoint of packet (%)
1	≈0.02	15	60	35
2	≈0.04	38	38	28
3	≈0.02	49	26	24
4	≈0.10	60	15	19
5	≈0.02	71	4	10

Experimental data and modelling

Results from a separate flexible pile centrifuge test on soft soil were modelled using the methods discussed in the previous section, to compare the predicted BM profiles. Note that multiple campaigns of centrifuge testing were performed using the same reconstituted natural material, for which minor changes in sample preparation led to modest changes in soil properties. However, in all cases, the relevant parameters for the test being analysed are used. A reconstituted carbonate silt of low plasticity (PI = 22%) was used, normally consolidated in-flight at an acceleration of 80g. This particular silt was chosen because the reconstitution process leads to a soil with properties that are broadly comparable to deep water clay. The pile was made of T6 6061 Aluminium and the prototype pile external diameter, embedment depth, and height of the imposed displacement above the mudline were 1.114, 18.24, and 3.36 m, respectively. Tube samples were prepared from the same slurry and consolidated in tubes to a vertical pressure of 30 kPa, representing an embedment depth of ~6.0 m. From consolidated anisotropically undrained simple shear tests (CK_0U) using a Berkeley apparatus on these samples, the soil strength gradient with depth was calculated as k_{su} = 1.66 kPa/m. The sensitivity was measured with an in-flight T-bar test as S_t = 5. The experimental setup and the corresponding one-dimensional finite element Lateral Analysis of Piles "LAP" (Doherty 2017) model are shown in Fig. 6. Further details are found in Guevara et al. (2022*a*).

BMs were obtained at strain gauge locations along the pile. The displacement imposed at the hinge level followed the sequence shown in Fig. 7, and was measured with a pair of lasers (Fig. 6). The motion sequence consisted of five packets of varying amplitude cyclic movement, triangular in time, without consolidation periods in between. The number of cycles applied for each packet of cyclic amplitude is also shown in Fig. 7. Note that the fourth packet of cyclic amplitude was performed at half the frequency of the other packets, due to actuator speed limitations. The sequence was designed to demonstrate loading-history effects on the BM profile by revealing differences in the response during the first, third, and fifth packets of cycles, which all had the same displacement amplitude of ≈0.02d at the hinge level. The time shown in Fig. 7 is scaled for consolidation effects, by multiplying model time by n_g^2 (Garnier et al. 2007), with n_g being the centrifuge acceleration (n_g = 80 for this test).

The pile was modelled numerically using the software LAP (Doherty 2017) and the p–y methods presented in the previous section. The same p_u profile was applied for all cases, following the ISO method originally published in Jeanjean et al. (2017). A no-gapping condition was assumed, which is consistent with the undrained strength gradient k_{su}. The p–y curves for each method were determined at 1 m intervals, down to 20 m below the mudline, and LAP interpolates between these at intermediate nodes. The pile flexural stiffness, based on the scaled dimensions, was 889 MN.m^2 and the pile–soil interface was assumed to be partially rough (Guevara et al. 2022*a*). The head displacement sequence recorded in the tests was imposed at the pile top in the LAP model and the soil response was modelled at each timestep of the analysis.

For the PICSI method, an initial set of monotonic p–y curves were determined by scaling from simple shear tests following Zhang and Andersen (2017). The scaling factors ξ_1 = 2.8 and ξ_2 = 2.0 were used to convert the strain from the simple shear tests to normalised displacement (y/d) for the p–y curves. The factor ξ_2 = 2.0 is slightly larger than the value

Fig. 9. ISO draft fatigue *p*–*y* curve and proposed simplified *p*–*y* curve.

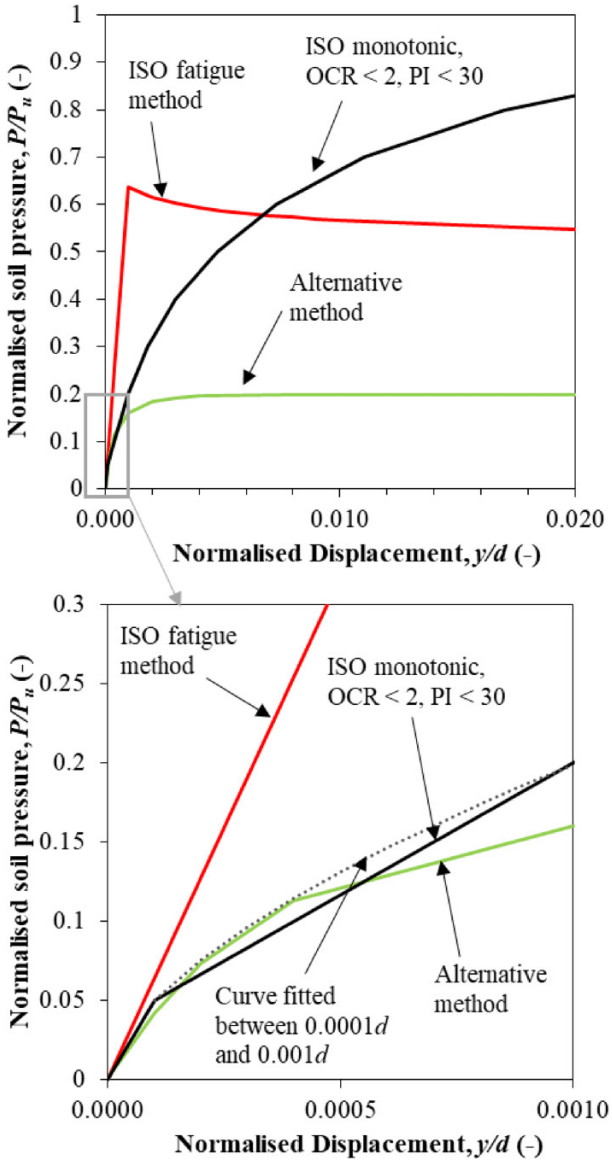

of 1.6 recommended by Zhang and Andersen (2017) and was selected as a calibration parameter to adjust the *p*–*y* stiffness at small strains, improving the first-cycle BM profiles (Fig. 8).

This monotonic *p*–*y* curve was transformed into a PI system of springs and sliders at each pile node for the PICSI model following the Guevara et al. (2023) calibration process and modified fully remoulded state envelope (Table 1).

The dissipation, by the end of the test, of the pore pressures generated in the cycle at midpoint of each packet has been calculated using the Osman and Randolph (2012) solution and is presented in Table 2. The coefficient of consolidation used in the calculations is $c_h = 1$ m^2/year, as previously documented by Guevara et al. (2023) and Chow et al. (2020) for this material. It is noted that, by the end of the test, 35% of the pore pressures generated in the cycle midpoint of the first packet would be dissipated, yet this packet generates the least damage (and hence the least pore pressures). Therefore, although some dissipation is produced during the test, it is not sufficient to explore the recovery aspects of PICSI, and hence only its damage modelling capabilities are observed when modelling this test.

The ISO fatigue *p*–*y* curves were derived using eq. 4 and the calculated p_u. The parameters A_s and B_s were assigned values of 0.45 and 0.05, respectively, as suggested in Zakeri et al. (2019) for clays with $s_u < 40$ kPa.

The *p*–*y* curves from the alternative method proposed in this paper were generated using eqs. 8–11, with $K_{max} = 495$ (eq. 7), and $n = 0.4$ and $y_{rem}/d = 0.05$, as derived earlier from separate rigid pile centrifuge tests. The measured sensitivity of the carbonate silt used in the rigid pile centrifuge tests ($S_t = 3.3$) differed slightly from the flexible pile tests ($S_t = 5$), while the measured $k_{su} \approx 1.65$ kPa/m was the same. For consistency, with the soil measurements, $S_t = 5$ was used to determine p_{rem}/p_u for eqs. 8 and 10. The results from this approach are labelled as the alternative method.

Comparison of methods

The ISO and alternative method fatigue *p*–*y* curves are shown in Fig. 9 alongside the default monotonic ISO *p*–*y* curve for a soil of OCR < 2 and plasticity index < 30.

The ISO curve is stiffest up to $y = 0.001d$, with an initial stiffness up to three times the monotonic value at displacements below this level. This cannot be justified based on damping effects, as these are directly proportional to strain level and are thus small for displacements in that order of magnitude (Stokoe et al. 1980; Vucetic and Dobri 1991).

The alternative method *p*–*y* curve is similar to the monotonic ISO *p*–*y* curve for $y < 0.001d$, and then softens to a plateau at a $p/p_u = 1/S_t$. Since the ISO monotonic *p*–*y* curve discretisation jumps from $p/p_u = 5\%$ ($y/d = 0.0001$) to $p/p_u = 20\%$ ($y/d = 0.001$), a curve has been fitted (shown dotted in Fig. 9) to illustrate the match with the alternative method—which is reasonable. This is encouraging since the alternative method was derived independently from the ISO guidance and is based directly on G_{max}, s_u, and S_t, but is reasonable since damage is not expected at displacements where the soil behaves almost elastically.

The BM profiles at the peak positive displacement for the cycles at the start and end of each packet in the sequence are shown in Fig. 10 (N = 1–700) and Fig. 11 (N = 701–900), including both the measured data and the three predictions.

At $N = 1$ the BM profile generated from the ISO fatigue *p*–*y* curve appears overly stiff, resulting in higher pile head lateral force, and therefore an overprediction of BMs above and below the mudline, and an underprediction at depth. This trend is also observed for all other cycles in both Figs. 10 and 11, even at the start of the larger amplitude packets where the soil has not reached "steady-state" (and hence should be stiffer than predicted by the fatigue curves).

The alternative method underpredicts the BMs at the start of each larger amplitude packet (N = 1, 401, 701), which is consistent with the method being developed for a fully remoulded or steady state. The method predicts the BMs for cycles 400, 600, and 800 better, which represent steady state cycles for packets 1, 2, and 4. For N = 601, 700, 801, and 900—

Fig. 10. Bending moment profiles for $N = 1$ to 700.

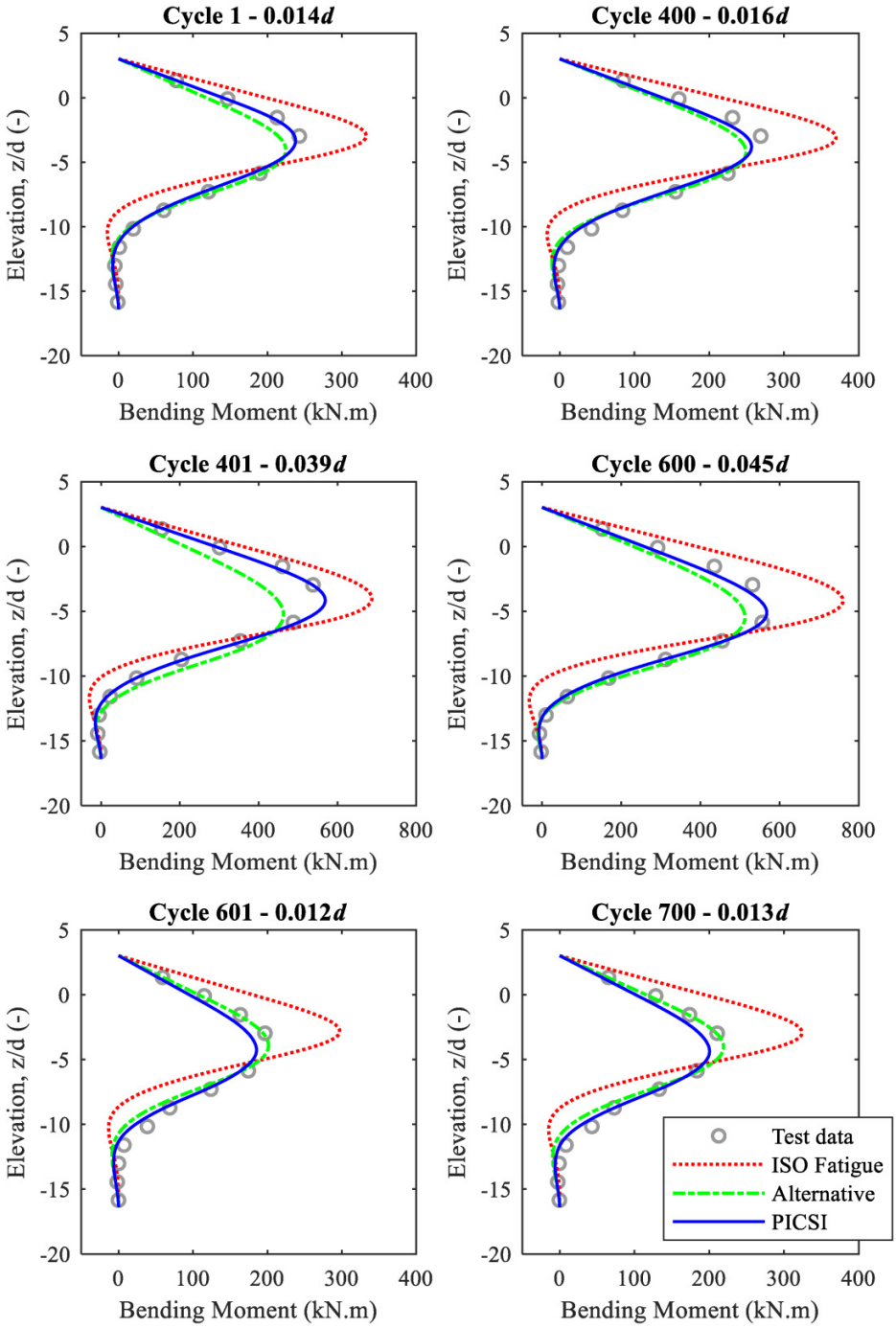

which are influenced by previous larger amplitude cycles—the method also accurately predicts the BM profile. The PICSI model accurately tracks the BM profiles from cycles 1 to 800 but appears to overpredict the magnitude of the BMs for cycles 801 and 900.

The accuracy of the BM calculated from each method is summarised in Fig. 12, discretised into shallow, peak, and deep zones. The different zones were determined based on their position relative to the depth where the peak BM is observed, $(z/d)_{peak}$. Since this depth varies depending on the head displacement, it was nominally selected as the elevation of the strain gauge that reported the highest BM for the largest amplitude cycle ($N = 800$), which gave $(z/d)_{peak} \sim -5.9$. The shallow zone groups the BM for depths above $0.25(z/d)_{peak}$, the peak zone groups the BM for depths between $0.25(z/d)_{peak}$ and $1.5(z/d)_{peak}$, while the deep zone groups all BM observations below the peak zone.

For the fully remoulded "steady-state" approaches (i.e., ISO fatigue and alternative method proposed in this paper), only the last cycle of each amplitude packet is plotted, whereas for

Fig. 11. Bending moment profiles for $N = 701$ to 900.

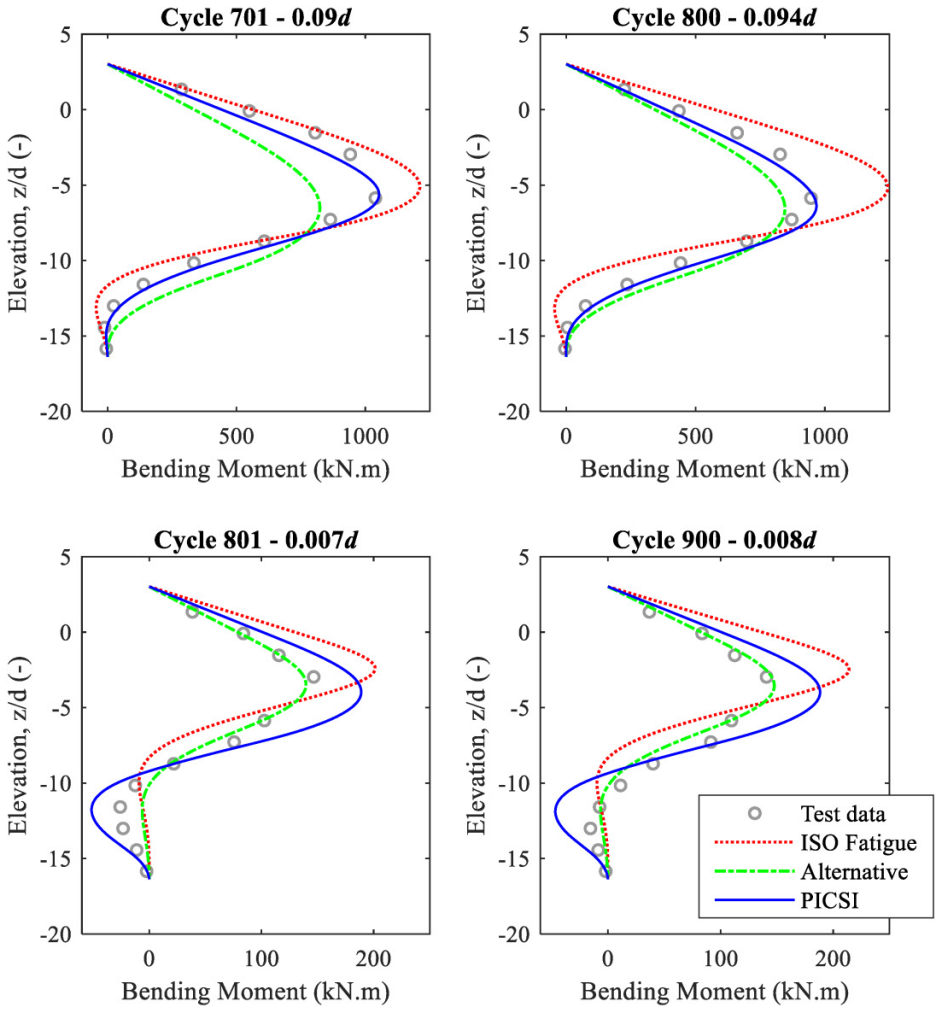

the PICSI method the start and end cycles of each packet are plotted—with the hollow markers indicating a BM measured at the end cycle of a packet, and filled markers indicating a BM measured at the start of a packet. To illustrate the level of agreement, a range of ±25% is shown in Fig. 12.

For the shallow zone, the BMs calculated using the ISO fatigue *p*–*y* curves overpredict all measured BMs by more than 25%. In contrast, calculations using the alternative method consistently lie within the 25% band. However, there is a weak trend for the BM to be underpredicted as the magnitude increases. The PICSI method leads to predictions that lie closest to the observations throughout.

For the peak BM zone, the ISO fatigue method also consistently overpredicts the measured values, particularly for the higher BMs, with some scatter seen at low BM. Both the PICSI and alternative methods accurately predict the BMs in this zone.

For the deep zone, broadly opposite observations to the shallow zone can be made. Importantly, the BMs calculated using the ISO fatigue method underpredict the measured BMs in the deep zone. For modest BMs, which are expected to dominate most fatigue assessments, the underprediction is by a factor of up to four.

Changing bending moment profile due to load history

As mentioned in the introduction, fatigue analyses involve summation of damage around the hotspots through different operating conditions. The lowest fatigue life of any of the analysed components limits the design and determines the fatigue life of the system.

Any change in the BM profile, shifting upwards or downwards, under the same amplitude of movement but at different stages in the operating life, will affect the system fatigue. When the upper metres of soil become remoulded due to cycling, the BM profile shifts downwards as strength needs to be mobilised by soil at lower depths. This pushes the profile of stress range lower down the pile, and would not be accounted for if the same soil spring is assumed to apply throughout the fatigue analysis and the system operating life.

The impact of the load history on the BM profile is illustrated in Fig. 13. A normalised BM range is used, defined as per eq. 13, on a colour scale to show the variation throughout all cycles in the sequence.

$$\frac{\Delta M}{\Delta M_{\max}} = \frac{M_{\text{peak } N_{zi}} - M_{\text{trough } N_{zi}}}{\max\left(M_{\text{peak } N_{zi}} - M_{\text{trough } N_{zi}}\right)_z} \quad (13)$$

Fig. 12. Calculated versus measured bending moments.

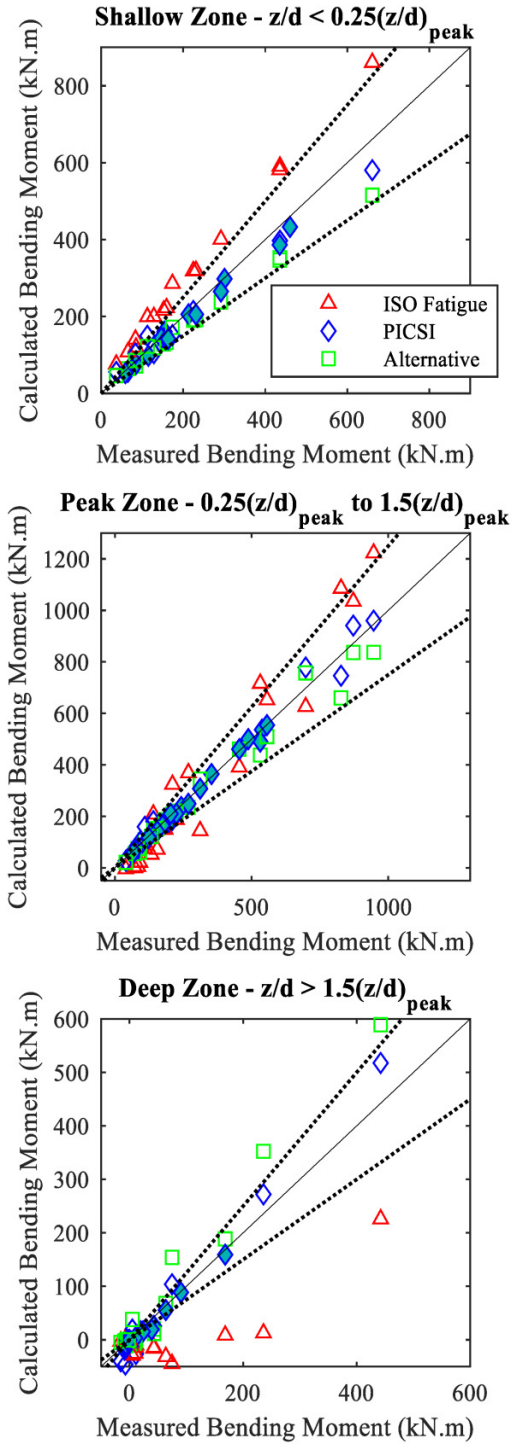

where $M_{\text{peak }Nzi}$ is the BM at depth z_i, for the positive peak head displacement in cycle N, $M_{\text{trough }Nzi}$ is the BM at depth z_i, for the negative peak head displacement in cycle N, and $\max(M_{\text{peak }Nzi} - M_{\text{trough }Nzi})_z$ is the maximum range of BM at any depth for cycle N.

This choice of normalisation allows the depth of the peak BM amplitude to be visualised, without the influence of the different cyclic amplitudes in each packet.

Figure 13 also shows the depth of the peak BM range as a black continuous line. If the load history did not affect the BM profile, the location of the peak BM range would be constant for cycles of the same amplitude, such as those from packets 1, 3, and 5. However, Fig. 13 shows that the largest BM range at the end of the third packet occurs at a greater depth than at the end of the first packet. Furthermore, the largest BM range at the end of the fifth packet is at an even greater depth. This demonstrates that the BM profile progresses downwards as the soil softens due to larger amplitude packets of cyclic loading and does not return up to the original position when the loading reduces.

This impact is also evident in Fig. 14, which shows profiles of normalised and nonnormalised BM range for the first and last cycle in each packet of the sequence. The colours used to identify the BM range profiles in Fig. 14 are the same colours shown for each packet in the displacement sequence at the hinge level from Fig. 13*a*. The depth of the maximum BM range moves downwards during each cycle packet and this effect is partly preserved when the amplitude is reduced after larger packets. Consequently, the BM profiles in packets 1, 3, and 5 differ due to the intervening cycles.

Fatigue damage accumulation

Fatigue damage along the pile during the loading sequence was estimated from the stress ranges obtained using each of the three p–y curve cases and from the measured data. The stress range at each depth was determined from the magnitude of BM range in each cycle. The fatigue damage was found from the stress range and number of cycles using an S–N curve. A stress concentration factor, SCF, of 10 was used along the pile, to amplify the stresses and visualise the damage over a longer sector of the pile. This adjustment represents the typical stress levels associated with hot spots and was not so extreme that fatigue failure was calculated.

For this example, the S–N curve for T6 6061 Aluminium proposed by Yahr (1997) was used, given that this was the material used for the model pile—although the same conclusions would be reached if steel material was considered, as per real piles and conductors. In practice, fatigue life estimates use a range of SCFs paired with different S–N curves, usually following DNV GL (2019) but depending on the characteristics of each hotspot or location of interest.

Total fatigue damage was then estimated using the Palgrem–Miner linear cumulative damage method (Miner 1945), leading to the fatigue damage profiles shown in Fig. 15 for each packet of cycles. The Yahr (1997) S–N curve has a cut-off at ≈96 MPa, below which it is assumed there is no fatigue damage accumulation—hence locations where this stress was not reached, even with the SCF, are not plotted in Fig. 15.

The key observation from Fig. 15 is that the ISO method consistently over-predicts fatigue at shallow elevations ($z/d < 5$), while underpredicting it at deeper depths. Meanwhile, the alternative and PICSI methods provide more accurate estimates of fatigue, matching well the shape of the measured fatigue profile—with the difference between these two approaches being that the PICSI predictions follow the test

Fig. 13. Normalised bending moment range with depth per cycle number.

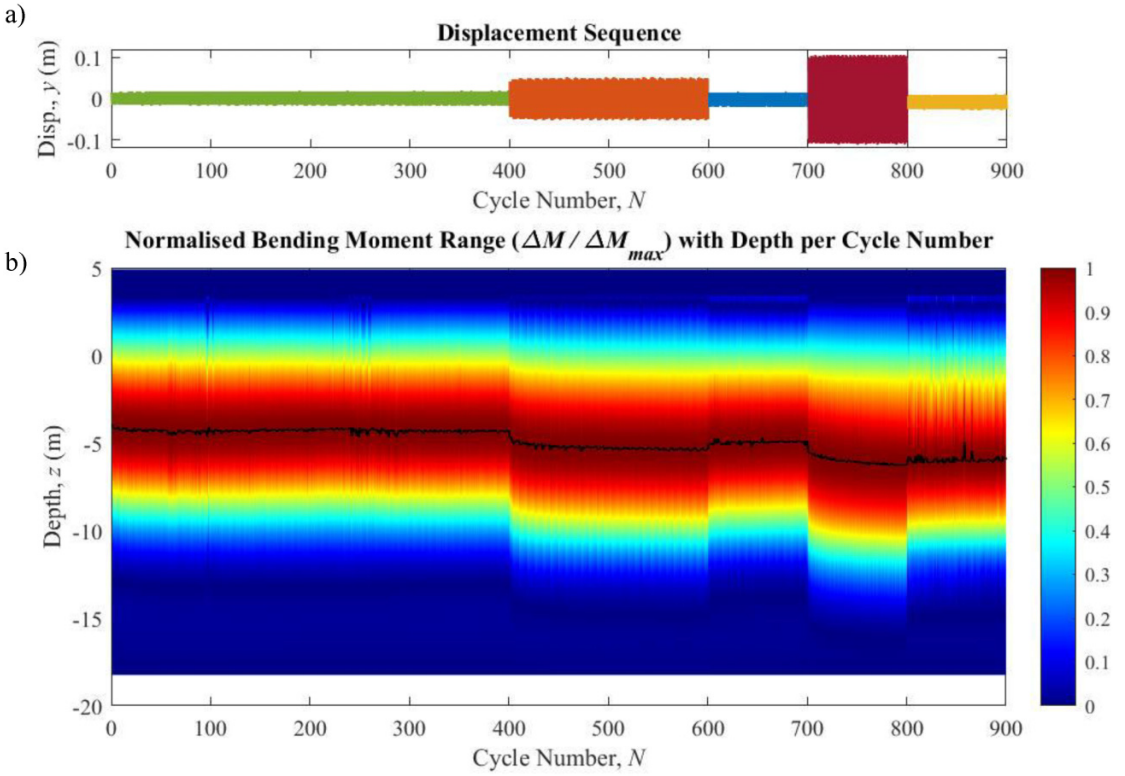

Fig. 14. Profiles of bending moment range for cycles at the start (solid line) and end (dotted line) of each packet: (*a*) normalised and (*b*) non-normalised.

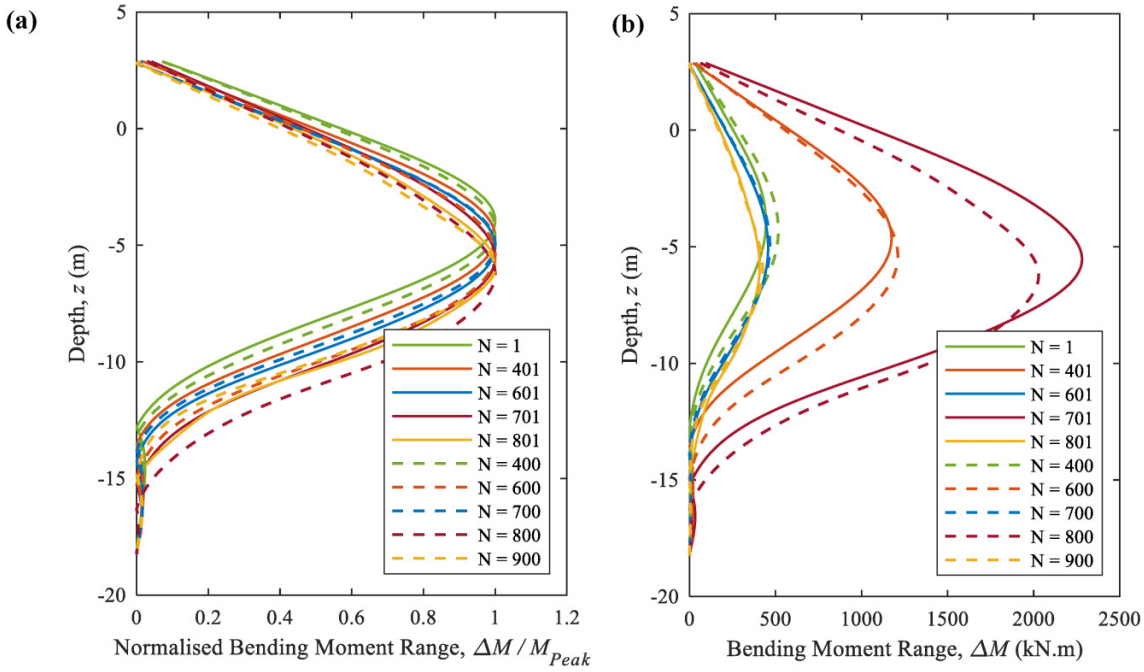

observation of a progressive downwards movement of the fatigue profile through successive packets.

When comparing between multiple packets of the same amplitude (i.e., packets 1, 3, and 5), Fig. 15 shows that the PICSI method predicts the changing damage most accurately. In comparison, the alternative method shows reasonable accuracy although some divergence is evident for the fifth packet. The ISO method overestimates the damage on the upper 5 *d* below the mudline, and underestimates it below this depth.

Fig. 15. Profiles of fatigue damage during each cyclic packet.

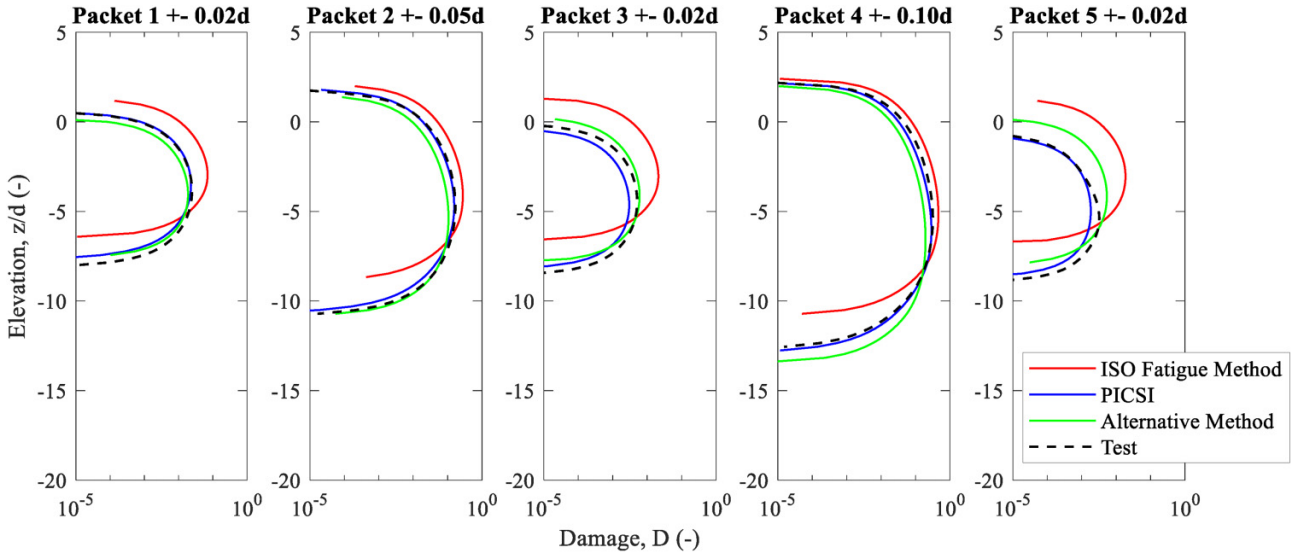

Fig. 16. Profiles of fatigue damage during smaller amplitude packets (≈0.02*d* at the hinge level).

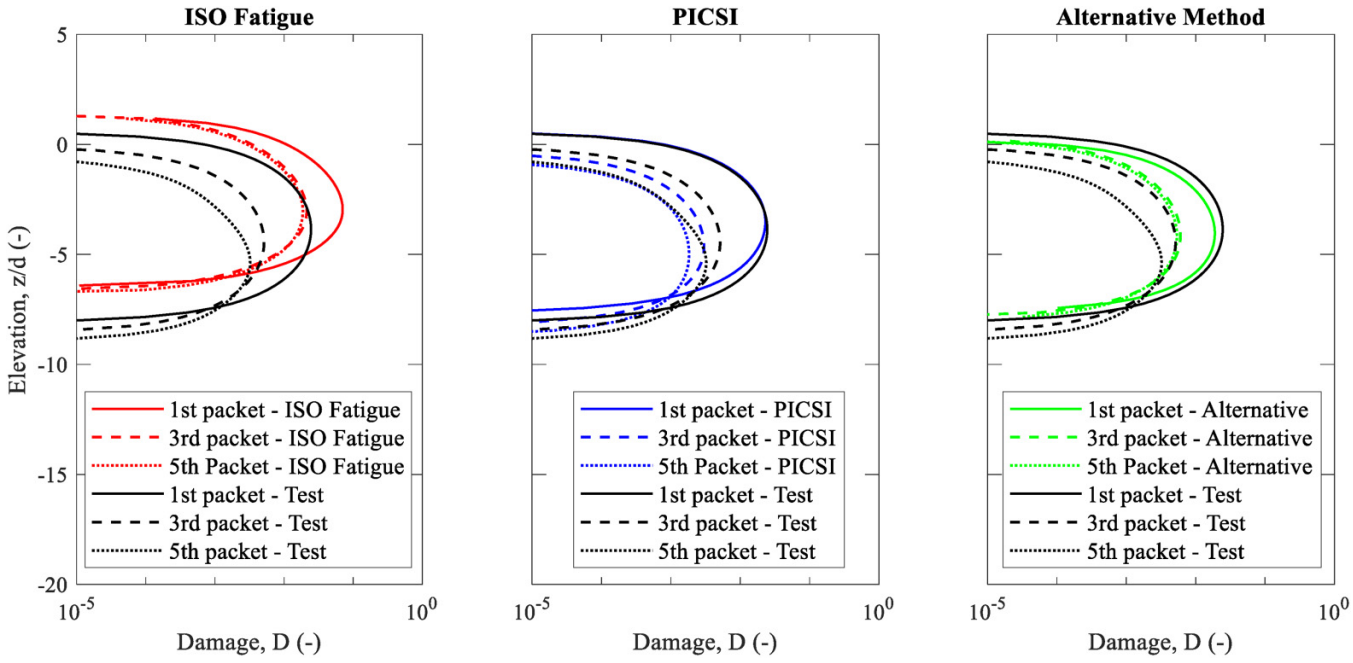

An alternate visualisation is provided in Fig. 16, focusing on damage arising from packets 1, 3, and 5 by comparing the different *p*–*y* curve methods with the measured damage. There is a progressive downwards shift of the damage profile from the test results after each of the larger cyclic amplitude packets. PICSI tracks this shift in BM, whereas the alternative and ISO methods do not have such a history-dependency.

A summary of the fatigue predictions is shown in Fig. 17, with the calculated maximum fatigue damage for each method in each packet being normalised by the measured maximum fatigue damage. The ISO method is consistently over-conservative, particularly for the smaller-amplitude packets (1, 3, and 5), for which the predicted damage is 3–6 times greater than the measurements. In contrast, the PICSI and alternative methods provide more accurate estimates, although both on average slightly underestimate the damage. In addition to the accuracy of the estimated maximum damage, it is important to highlight the accuracy by which the depth of this point is estimated. The ISO method consistently predicts that the peak damage will occur at a shallower position compared to the measurements, due to the erroneously high stiffness (Figs. 15 and 16). This systematic error contrasts with the other two methods, which both capture the shape of the fatigue profile more accurately and locate the maximum fatigue hotspot to within a depth of 1 m of the true value.

Fig. 17. Summary of fatigue estimates relative to measured data.

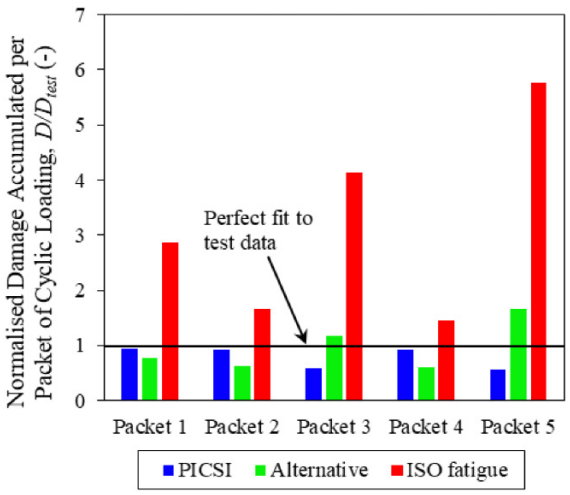

Discussion

The study highlights how the estimated BM profile of a pile is affected by adopting a *p*–*y* response that is too stiff, including the new ISO fatigue curves. Such curves lead to shallow overprediction and deeper underprediction of the BM, resulting in incorrect fatigue life estimates.

The opposite conclusions apply for *p*–*y* curves that are too soft. For the alternative method proposed in this paper, slightly lower BMs are predicted for the upper sections of the system, with slightly higher predictions in the lower sections. This could be because the reduction factor of $1/S_t$ imposed for p_{rem}/p_u in eqs. 8 and 10 is too onerous, and perhaps a lower reduction in p_u is appropriate, particularly at depth where the movements are smaller. Further testing would help resolve this hypothesis. Despite these observations, the alternative method proposed in this paper provides a better fit overall to the new data in this study, and also to the previously-published data on which the ISO fatigue curves were based (Fig. 5).

The PICSI model accurately tracks the changing *p*–*y* response due to progressive cyclic remoulding and therefore captures well the changing BM profile through the cyclic sequence of the test. This study highlights that loading history has an impact on the BM profile with the result that large amplitude cycles tend to shift the BM profile downwards (Figs. 13 and 14). This increases the magnitude of stress further down in the pile and can only be properly modelled using a *p*–*y* model that accounts for load history—although calibrating, implementing, and running such a model requires additional work and input data, which in many cases may not be available. Nonetheless, it may represent the most appropriate approach when dealing with soils of high sensitivity or permeability, or where previous pore pressures due to cycling have been dissipated and the soil has hardened. As noted before, the test duration was too short for significant dissipation of pore pressure following cyclic loading so only the damage modelling capabilities of PICSI are explored. However, PICSI was able to model strength and stiffness recovery due to pore pressure dissipation, which could be more impactful for longer cycling periods, or for soils with higher coefficient of consolidation. A further application of PICSI could be for reassessing the fatigue life of well system components when a large amplitude storm event has occurred and disconnecting the system was not possible.

Based on findings in this paper the alternative method is proposed for cases where the "fully remoulded" condition dominates the fatigue life, with PICSI being suitable if the full loading history can be modelled.

Conclusions

This paper presents an alternative *p*–*y* curve method for fatigue analysis of conductors that links laboratory-measured soil parameters to pile–soil stiffness using rigorous theoretical concepts. The alternative approach leads to *p*–*y* curves that give good agreement with new and previously-published data on the *p*–*y* stiffness (including the data from which the ISO fatigue *p*–*y* curves were based), and a numerical back-analysis of centrifuge model test data shows that it predicts the measured BMs within ±25%.

In comparison, the ISO fatigue *p*–*y* curves are much stiffer, overpredicting the BM (and therefore stress) in the upper sections of the conductor, and underpredicting them in the lower sections.

Comparisons with experimental data show that the PICSI model predicts the BMs most accurately over the full test sequence, and can capture the movement of the fatigue hotspot that smears the fatigue damage down the pile. However, calibrating and implementing the PICSI model requires additional work and data, which in many cases may not be available.

Future work could explore the validation of the method proposed in this paper with additional experimental data, and in different soil types to those investigated in this study.

On the basis of this study, it is recommended that the new alternative model is adopted for fatigue life estimation of drilling conductor systems, while in some situations the PICSI approach may be merited for more detailed analysis.

List of symbols

d	pile diameter
G	shear modulus
G_{max}	Small-strain shear modulus
k	secant stiffness of a *p*–*y* curve at any given point
$k_{p\text{-}p}$	peak-to-peak secant stiffness within a loop
k_{su}	soil strength gradient with depth
K	normalised "steady-state" secant stiffness
K_{max}	normalised maximum secant *p*–*y* stiffness at displacements in the elastic range
L	pile length
$M_{peak\ Nzi}$	bending moment at depth z_i, for the positive peak head displacement in cycle N
$M_{trough\ Nzi}$	bending moment at depth z_i, for the negative peak head displacement in cycle N

n	parameter that determines the shape of the pressure–displacement response
N	number of cycles
N_p	lateral bearing capacity factor
p	nominal lateral pressure on the pile
p_f	lateral soil pressure for fatigue actions
p_{fa}	normalised soil response for fatigue actions
p_{rem}/p_u	normalised fully remoulded soil resistance, equal to $1/S_t$
p_u	ultimate lateral soil reaction pressure
P	soil resistance per unit length of pile
s_u	undrained shear strength of soil
S_t	soil sensitivity
y	lateral displacement
y_{rem}/d	normalised displacement at which p_{rem}/p_u is reached
$(z/d)_{peak}$	position relative to the depth where the peak bending moment is observed
ΔM	bending moment range
ΔM_{max}	maximum bending moment range along the pile
Δp	range of lateral soil reaction
Δy	lateral peak-to-peak movement amplitude
δy	increment of lateral displacement
δt	interval of time
γ	shear strain
ξ_1 and ξ_2	scaling factors used to convert the strain from the simple shear tests to normalised displacement (y/d) for p–y curves

Acknowledgements

The authors acknowledge the funding and execution of laboratory tests from the Norwegian Geotechnical Institute. The first author is supported by the ARC Industrial Transformation Research Hub for Offshore Floating Facilities that is funded by the Australian Research Council, Shell Australia, Woodside Energy, Bureau Veritas, and Lloyd's Register (IH140100012). The third author leads the Shell Chair in Offshore Engineering research team at The University of Western Australia, which is sponsored by Shell Australia. The fourth author acknowledges the support of the EPSRC Offshore Renewable Energy Supergen Hub (EPSRC grant ref. EP/Y016297/1).

Article information

History dates

Received: 17 July 2024
Accepted: 5 May 2025
Accepted manuscript online: 23 May 2025
Version of record online: 24 July 2025

Data availability

Data generated or analyzed during this study are not publicly available due to confidentiality agreement with research collaborators but are available from the corresponding author on reasonable request.

Author information

Author ORCIDs

M. Guevara https://orcid.org/0000-0002-2923-9045
J.P. Doherty https://orcid.org/0000-0002-8939-6384
P.G. Watson https://orcid.org/0000-0002-4548-8455
D.J. White https://orcid.org/0000-0002-2968-582X

Author contributions

Conceptualization: MG, JD, DW
Formal analysis: MG, PW, DW
Investigation: MG
Methodology: MG, JD, PW
Resources: PW
Software: JD
Supervision: JD, PW, DW
Visualization: MG, DW
Writing – original draft: MG
Writing – review & editing: JD, PW, DW

Competing interests

The authors declare there are no competing interests.

References

Baguelin, F., Frank, R., and Saïd, Y.H. 1977. Theoretical study of lateral reaction mechanism of piles. Géotechnique, **27**(3): 405–434. doi:10.1680/geot.1977.27.3.405.

Bransby, M.F. 1999. Selection of p-y curves for the design of single laterally loaded piles. International Journal for Numerical and Analytical Methods in Geomechanics, **23**(15): 1909–1926. doi:10.1002/(sici)1096-9853(19991225)23:15⟨1909::aid-nag26⟩3.0.co;2-l.

Burd, H.J., Taborda, D.M.G., Zdravković, L., Abadie, C.N., Byrne, B.W., Houlsby, G.T., et al. 2019. PISA design model for monopiles for offshore wind turbines: application to a marine sand. Géotechnique, **70**(11): 1048–1066. doi:10.1680/jgeot.18.p.277.

Chow, S.H., O'Loughlin, C., Zhou, Z., White, D.J., and Randolph, M.F. 2020. Penetrometer testing in a calcareous silt to explore changes in soil strength. Géotechnique, **70**(12): 1160–1173. doi:10.1680/jgeot.19.P.069.

DNV GL. 2019. DNVGL-RP-C203: fatigue design of offshore steel structures. Edition 2019, Amended 2021.

Doherty, J. 2017. A web based application for the lateral analysis of pile (LAP) foundations. *In* Proceedings of the ASME 2017 36th International Conference on Ocean, Offshore and Arctic Engineering. Vol. 9. Offshore Geotechnics, ASME, Trondheim, Norway.

Doherty, J., White, D.J., Watson, P.G., and Grime, A. 2019. Life cycle changes in p-y stiffness for a conductor pile installed in carbonate silt. *In* Proceedings of the 1st Vietnam Symposium on Advances in Offshore Engineering: VSOE 2018. Lecture notes in civil engineering. Springer, Singapore. pp. 362–368.

Garnier, J., Gaudin, C., Springman, S.M., Culligan, P.J., Goodings, D., Phillips, R., et al. 2007. Catalogue of scaling laws and similitude questions in geotechnical centrifuge modelling. International Journal of Physical Modelling in Geotechnics, **7**: 01–23. doi:10.1680/ijpmg.2007.070301.

Guevara, M., Doherty, J.P., Watson, P.G., and White, D.J. 2020. Key features impacting soil-conductor lateral behaviour as illustrated by centrifuge tests. *In* Proceedings of the 4th International Sym-

posium on Frontiers in Offshore Geotechnics ISFOG 2020, Austin. pp. 1–10.
Guevara, M., Doherty, J.P., Watson, P.G., and White, D.J. 2021. Evolving soil-conductor stiffness due to multiple-episode cyclic loading. *In* Second Vietnam Symposium on Advances in Offshore Geotechnics, Ho Chi Minh City. pp. 1–8.
Guevara, M., Doherty, J.P., Gaudin, C., and Watson, P.G. 2022a. Evaluating uncertainty associated with engineering judgement in predicting the lateral response of conductors. Journal of Geotechnical and Geoenvironmental Engineering, **148**(5): 1–15. doi:10.1061/(asce)gt.1943-5606.0002759.
Guevara, M., Doherty, J., Watson, P., White, D., Boylan, N., and Teng, Y. 2022b. A comparison study of soil-conductor stiffness from centrifuge and laboratory testing. *In* Proceedings of the 20th International Conference on Soil Mechanics and Geotechnical Engineering, Sydney.
Guevara, M., Doherty, J., Watson, P., and White, D.J. 2023. A methodology to calibrate the PICSI cyclic p-y model using experimental results and optimisation. Ocean Engineering, **287**(115786): 115786. doi:10.1016/j.oceaneng.2023.115786.
ISO. 2016. Petroleum and natural gas industries–specific requirements for offshore structures–part 4: geotechnical and foundation design considerations. ISO 19901-4: 2016. International Standards Organisation, Geneva.
ISO/DIS. 2022. ISO/DIS 19901-4 Oil and gas industries including lower carbon energy–specific requirements for offshore structures–part 4 : geotechnical design considerations. Under development. Geneva.
Jeanjean, P. 2009. Re-assessment of P-Y curves for soft clays from centrifuge testing and finite element modeling. Offshore Technology Conference, Houston.
Jeanjean, P., Zhang, Y., Zakeri, A., Andersen, K.H., Gilbert, R., and Senanayake, A. 2017. A framework for monotonic p-y curves in clay. *In* Proceedings of the 8th International Conference of Offshore Site Investigation and Geotechnics, London. pp. 108–141.
Komolafe, O., and Aubeny, C. 2020. A p-y analysis of laterally loaded offshore-well conductors and piles installed in normally consolidated to lightly overconsolidated clays. Journal of Geotechnical and Geoenvironmental Engineering, **146**(6): 1–18. doi:10.1061/(ASCE)GT.1943-5606.0002249.
Miner, M. 1945. Cumulative damage in fatigue. Journal of Applied Mechanics, **12**: A159–A164. doi:10.1115/1.4009458.
Murff, J.D., and Hamilton, J.M. 1993. P-ultimate for undrained analysis of laterally loaded piles. Journal of Geotechnical Engineering, **119**(1): 91–107. doi:10.1061/(ASCE)0733-9410(1993)119:1(91).
Osman, A.S., and Randolph, M.F. 2012. Analytical solution for the consolidation around a laterally loaded pile. International Journal of Geomechanics, **12**(3): 199–208. doi:10.1061/(ASCE)GM.1943-5622.0000123.
Randolph, M.F., and Houlsby, G.T. 1984. The limiting pressure on a circular pile loaded laterally in cohesive soil. Géotechnique, **34**(4): 613–623. doi:10.1680/geot.1984.34.4.613.
Stokoe, K., Isenhower, W., and Hsu, J. 1980. Dynamic properties of offshore silty samples. *In* Proceedings of the Annual Offshore Technology Conference, Houston. pp. 289–302.
Vardanega, P., and Bolton, M. 2013. Stiffness of clays and silts: normalising shear modulus and shear strain. Journal of Geotechnical and Geoenvironmental Engineering, **139**(9): 1575–1589. doi:10.1061/(ASCE)GT.1943-5606.0000887.
Vucetic, M., and Dobri, R. 1991. Effect of soil plasticity on cyclic response. Journal of Geotechnical Engineering, **117**(1): 89–107. doi:10.1061/(ASCE)0733-9410(1991)117:1(89).
White, D.J., Doherty, J.P., Guevara, M., and Watson, P.G. 2022. A cyclic p-y model for the whole-life response of piles in soft clay. Computers and Geotechnics, **141**(104519): 1–11. doi:10.1016/j.compgeo.20210104519.
Wood, D.M. 1990. Soil behaviour and critical state soil mechanics. Soil behaviour and critical state soil mechanics, Cambridge University Press.
Yahr, G.T. 1997. Fatigue design curves for 6061-T6 aluminum. Journal of Pressure Vessel Technology, **119**(2): 211–215. doi:10.1115/1.2842286.
Yu, J., Huang, M., and Zhang, C. 2015. Three-dimensional upper-bound analysis for ultimate bearing capacity of laterally loaded rigid pile in undrained clay. Canadian Geotechnical Journal, **52**(11): 1775–1790. doi:10.1139/cgj-2014-0390.
Zakeri, A., Clukey, E.C., Kebadze, E.B., and Jeanjean, P. 2016. Fatigue analysis of offshore well conductors: part I–study overview and evaluation of series 1 centrifuge tests in normally consolidated to lightly over-consolidated kaolin clay. Applied Ocean Research, **57**: 78–95. doi:10.1016/j.apor.2016.03.002.
Zakeri, A., Sturm, H., Dyvik, R., and Jeanjean, P. 2017. Development of novel apparatus to obtain soil resistance–displacement relationship for well conductor fatigue analysis. Canadian Geotechnical Journal, **54**(10): 1435–1446. doi:10.1139/cgj-2016-0528.
Zakeri, A., Sturm, H., and Jeanjean, P. 2019. Validation and extension of soil response framework for fatigue analysis of offshore wells and piles. Offshore Technology Conference, (OTC 29236).
Zhang, White, D., and Randolph, M. 2011. Centrifuge modeling of the cyclic lateral response of a rigid pile in soft clay. Journal of Geotechnical and Geoenvironmental Engineering, **137**(7): 717–729. doi:10.1061/(ASCE)GT.1943-5606.0000482.
Zhang, Y., and Andersen, K.H. 2017. Scaling of lateral pile p-y response in clay from laboratory stress-strain curves. Marine Structures, **53**: 124–135. doi:10.1016/j.marstruc.2017.02.002.
Zhang, Y., Andersen, K.H., and Tedesco, G. 2016. Ultimate bearing capacity of laterally loaded piles in clay–some practical considerations. Marine Structures, **50**(February 2017): 260–275. doi:10.1016/j.marstruc.2016.09.002.